LETTER • OPEN ACCESS

How atmospheric humidity drives the outgoing longwave radiation–surface temperature relationship and inter-model spread

To cite this article: Jing Feng *et al* 2023 *Environ. Res. Lett.* **18** 104033

View the article online for updates and enhancements.

ENVIRONMENTAL RESEARCH
LETTERS

LETTER

How atmospheric humidity drives the outgoing longwave radiation–surface temperature relationship and inter-model spread

Jing Feng[1,][*] ![ORCID], David Paynter[2], Chenggong Wang[1] ![ORCID] and Raymond Menzel[2] ![ORCID]

[1] Atmospheric and Oceanic Sciences Program, Princeton University, 300 Forrestal Road, Princeton, NJ 08540-6654, United States of America
[2] Geophysical Fluid Dynamics Laboratory, 201 Forrestal Road, Princeton, NJ 08540-6649, United States of America
[*] Author to whom any correspondence should be addressed.

E-mail: jing.feng@princeton.edu

Abstract

The Earth's global radiation budget depends critically on the relationship between outgoing longwave radiation (OLR) and surface temperature (T_s). Using the fifth generation of European ReAnalysis dataset, we find that although OLR appears to be linearly dependent on T_s over a wide range, there are significant deviations from the linearity in the OLR–T_s relationship for regions warmer than 270 K T_s, which covers 89% of the surface of Earth. While the AMIP runs of CMIP6 models largely capture the overall OLR–T_s relationship, considerable discrepancies are found in clear-sky OLR at given T_s ranges. In this study, we investigate physical mechanisms that control the clear-sky OLR–T_s relationship seen in reanalysis and CMIP6 models by using accurate radiative transfer calculations. Our study identifies three key mechanisms to explain both the linearity and departure from linearity of the clear-sky OLR–T_s relationship. The first is a surface contribution, controlled by the thermal emission of the surface and the infrared opacity of the atmosphere, accounting for 60% of the observed clear-sky OLR–T_s linear slope. The second is changes in atmospheric emission induced by a foreign pressure effect on water vapor and other greenhouse gases, which accounts for 30% of the linear slope in a clear-sky condition. The third is changes in atmospheric emission induced by variations in relative humidity (RH), particularly in the mid-troposphere (250 to 750 hPa), which determines the non-linearity in the clear-sky OLR–T_s relationship and adds to the remaining 10% of the slope. The inter-model spread in mid-tropospheric RH explains a large fraction of the differences in clear-sky OLR across CMIP6 models at given surface temperatures. Furthermore, the three key mechanisms outlined here apply to the OLR–T_s relationship in all-sky conditions: clouds disguise the surface contribution but increase the atmospheric contribution, retaining a similar linear slope to the clear-sky condition while amplifying the non-linear curvature.

1. Introduction

The Earth's climate is regulated by the balance between the net incoming solar radiation and the outgoing longwave radiation (OLR) at the top-of-atmosphere (TOA). The surface of the Earth absorbs energy from incoming solar radiation and emits it in the longwave spectrum. Greenhouse gases and clouds trap the longwave energy radiated from the surface and re-radiate a fraction of it back to space, controlling the OLR at the TOA. Any additional energy input leads to an increase in the planet's surface temperature (T_s), which is a key quantity for evaluating the potential impacts of climate change on natural and human systems. Understanding the global relationship between OLR and T_s is vital for comprehending the radiation balance of the present-day climate and serves as an important indicator of future climate change.

The relationship between OLR and surface temperature (T_s) has been extensively studied using Earth system models and observational data. Previous

research has revealed that over Earth's surface, the OLR exhibits a near-linear relationship with T_s, characterized by a regression coefficient of approximately $2 \, W \, m^{-2} \, K^{-1}$ under clear-sky conditions [1–3]. This overall linearity is attributed to the trapping greenhouse effect of water vapor, which is predominantly influenced by T_s and offsets the growth curve in surface thermal emission [2]. However, it is important to note that OLR is not solely controlled by T_s, as it is also sensitive to atmospheric conditions and clouds [4–12]. Consequently, stronger deviations from a simple linear function over T_s are observed in subtropical and tropical regions [13], exhibiting seasonal [14] and inter-annual variations [15], as well as under global warming scenarios [16, 17].

This study investigates the key atmospheric conditions that shape the observed OLR over the present-day Earth in sections 2 and 3 and the causes of the inter-model spread in clear-sky OLR in section 4. The results are summarized and discussed in section 5.

2. The OLR–T_s relationship in the present-day Earth

OLR is jointly determined by the opacity of the atmosphere and the thermal emissions from both the surface and the atmosphere. Mathematically, it can be expressed as follows:

$$\text{OLR} = \int_v \mathfrak{T}_v B_v (T_s) \, dv + \int_v E_v \, dv \tag{1}$$
$$= \bar{\bar{\mathfrak{T}}} B (T_s) + E.$$

Here, T_s represents the surface temperature, v denotes the spectral frequency, $\mathfrak{T}_v$ and E_v refer to the transmittance through the entire atmosphere and atmospheric emission at each spectral frequency, respectively. $B_v(T_s)$ represents the black-body emission at frequency v, determined by Planck function of temperature at T_s. The terms $E = \int_v E_v \, dv$ and $B = \int_v B_v \, dv$ correspond to the integrated atmospheric emission and black-body emission, respectively. The term $\bar{\bar{\mathfrak{T}}} = \int_v \mathfrak{T}_v B_v (T_s) \, dv / B(T_s)$ represents the broadband transmittance, indicating the rate at which surface emission transmits to space.

With an increase in surface temperature (δT_s), OLR increases (δOLR) under the impact of the co-variation of atmospheric transmittance and emission with δT_s ($\delta \bar{\bar{\mathfrak{T}}}$ and δE). δOLR can be analytically decomposed as:

$$\delta \text{OLR} = \left(\bar{\bar{\mathfrak{T}}} + \delta \bar{\bar{\mathfrak{T}}} \right) B (T_s + \delta T_s) - \bar{\bar{\mathfrak{T}}} B (T_s) + \delta E$$
$$= \underbrace{\bar{\bar{\mathfrak{T}}} \left[B (T_s + \delta T_s) - B (T_s) \right]}_{\bar{\bar{\mathfrak{T}}} \delta B(T_s), \, \text{'surface'}} + \underbrace{B (T_s + \delta T_s) \delta \bar{\bar{\mathfrak{T}}} + \delta E}_{\text{'atmosphere'}}. \tag{2}$$

In this expression, the total δOLR is decomposed into a surface and an atmospheric contribution. The surface contribution, $\bar{\bar{\mathfrak{T}}} \delta B(T_s)$, represents the change in OLR resulting from a one-sided partial radiative perturbation in T_s. When $\delta T_s = 1 \, K$, this term is known as the 'surface Planck feedback' [2, 18, 19] or the surface temperature kernel [10, 20, 21] at local grid points. The atmospheric contribution, $B(T_s + \delta T_s) \delta \bar{\bar{\mathfrak{T}}} + \delta E$, accounts for changes in δOLR due to perturbations in atmospheric transmittance and emission.

Under clear-sky conditions, Koll and Cronin [2] proposed that the rate at which surface emission transmits to space determines δOLR_{cs} ($\delta \text{OLR}_{cs} \approx \bar{\bar{\mathfrak{T}}}_{cs} \delta B(T_s)$, where the subscript 'cs' denotes the clear-sky conditions hereinafter). They found that the clear-sky OLR tends to increase linearly with T_s rather than following a quadratic growth curve following $B(T_s)$, consistent with earlier studies [1]. They further suggested that this linearity arises because the quadratic growth curve rate in $B(T_s)$ is offset by the rate at which water vapor transmittance ($\sim \bar{\bar{\mathfrak{T}}}_{cs}$) decreases with T_s.
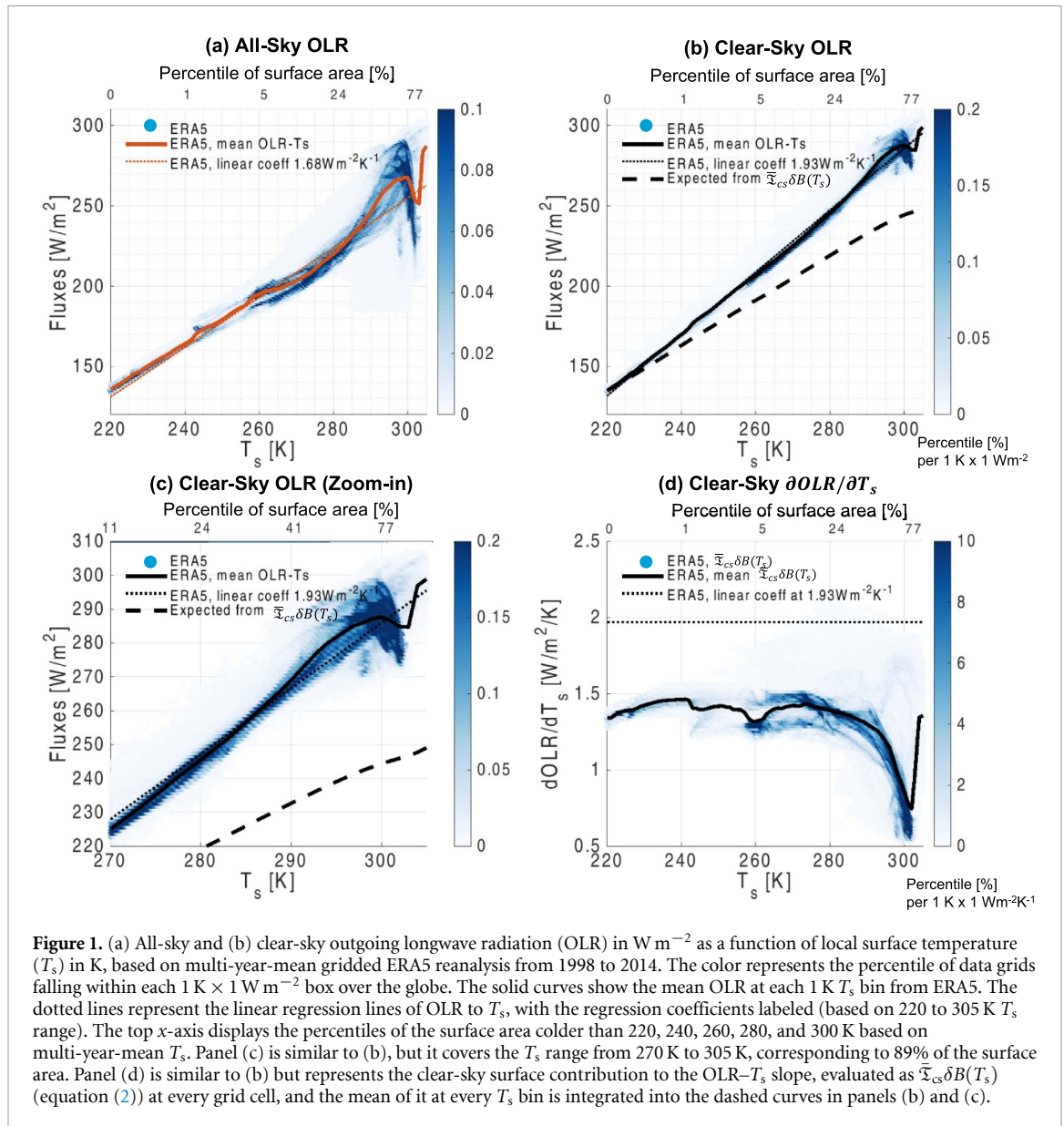
With the fifth generation of European ReAnalysis (ERA5 [22]) and line-by-line radiative transfer code, GPU-able Radiative Transfer code (GRTCODE, see appendix A), we can quantitatively examine how well the surface contribution can explain the observed and simulated OLR–T_s relationship on present-day Earth. Figure 1(a) shows the multi-year-mean OLR at every grid point on Earth as a function of T_s, based on the reanalysis, with the global distribution of multi-year-mean T_s presented in figure B1. Figure 1(a) suggests a near-linear increase in OLR with T_s, with more pronounced deviations from linearity in warmer regions. The linear regression slope is $1.93 \, W \, m^{-2} \, K^{-1}$ under clear-sky conditions, consistent with the findings of [2], and $1.68 \, W \, m^{-2} \, K^{-1}$ under all-sky conditions.

To compute $\bar{\bar{\mathfrak{T}}}_{cs} \delta B(T_s)$ at each grid point, we conduct line-by-line radiative transfer calculations using GRTCODE, as described in appendix A. Similar to figures 1(a) and (d) presents $\bar{\bar{\mathfrak{T}}}_{cs} \delta B(T_s)$ as a function of T_s. When compared to the observed clear-sky OLR–T_s slope, however, $\bar{\bar{\mathfrak{T}}}_{cs} \delta B(T_s)$ is significantly lower and decreases further with increasing T_s. The magnitude of $\bar{\bar{\mathfrak{T}}}_{cs} \delta B(T_s)$ is highly consistent with the line-by-line calculations conducted in [19] and the clear-sky surface temperature kernel available in publicly accessible datasets [10, 20].

To determine how much OLR increase from a reference T_s due to the surface contribution, we integrate $\bar{\bar{\mathfrak{T}}}$ (as a function of T_s) over $B(T_s)$ as:

$$\Delta \text{OLR}_{sfc} (T_i) = \int_{T_s = T_{s,\text{ref}}}^{T_s = T_i} \bar{\bar{\mathfrak{T}}} \, dB (T_s). \tag{3}$$

The derived $\Delta \text{OLR}_{cs, sfc}$ is then utilized to 'predict' the clear-sky OLR curve and is shown as the black dashed curve in figures 1(b) and (c), following [2],

Figure 1. (a) All-sky and (b) clear-sky outgoing longwave radiation (OLR) in W m^{-2} as a function of local surface temperature (T_s) in K, based on multi-year-mean gridded ERA5 reanalysis from 1998 to 2014. The color represents the percentile of data grids falling within each 1 K × 1 W m^{-2} box over the globe. The solid curves show the mean OLR at each 1 K T_s bin from ERA5. The dotted lines represent the linear regression lines of OLR to T_s, with the regression coefficients labeled (based on 220 to 305 K T_s range). The top x-axis displays the percentiles of the surface area colder than 220, 240, 260, 280, and 300 K based on multi-year-mean T_s. Panel (c) is similar to (b), but it covers the T_s range from 270 K to 305 K, corresponding to 89% of the surface area. Panel (d) is similar to (b) but represents the clear-sky surface contribution to the OLR–T_s slope, evaluated as $\bar{\bar{\mathfrak{T}}}_{cs}\delta B(T_s)$ (equation (2)) at every grid cell, and the mean of it at every T_s bin is integrated into the dashed curves in panels (b) and (c).

using reference T_s, $T_{s,\text{ref}}$, at 270 K. It becomes evident that $\Delta\text{OLR}_{\text{sfc}}$ significantly underestimates the OLR slope, regardless of the reference T_s (figures 1(b) and (c)). Thus, the surface contribution $\bar{\bar{\mathfrak{T}}}_{cs}\delta B(T_s)$ alone cannot explain the linear OLR–T_s relationship to first order. In particular, in regions with T_s above 290 K, $\bar{\bar{\mathfrak{T}}}_{cs}\delta B(T_s)$ is less than 1 W m^{-2} K^{-1} (figure 1(d)). Given its magnitude, which is much smaller than the actual OLR–T_s slope observed in these regions ($\sim$2 W m^{-2}K^{-1}) [3], $\bar{\bar{\mathfrak{T}}}_{cs}\delta B(T_s)$ cannot account for the observed OLR–T_s slope, regardless of the grid points being selected from this region. A significant portion of the linearity must arise from the atmospheric contribution in equation (2).

Although figure 1 shows a linear OLR–T_s relationship over a wide range of T_s, the near-perfect linearity mainly exists in the cold regions ($T_s < 270$ K), which only cover a small fraction (11%) of Earth

surface (see figure B1). As T_s increases, OLR deviates more strongly from a simple linear function over T_s, and this deviation pattern is well described by the mean OLR at each T_s bin shown as solid curves in figures 1(a)–(c). The mean OLR–T_s curves under clear-sky (figure 1(b)) and all-sky conditions (figure 1(a)) appear similar, with a steeper gradient in regions with T_s above 270 K, reaching a peak at 298 K, and then a dip at 302 K. From the sea surface temperature shown in figure B1, we find that the OLR peak is reached in the subtropical ocean and tropical cold pool, corresponding to dry, subsidence region. The dip is reached in the tropical warm pool, corresponding to moist, convective regions. The observed OLR curvature cannot be explained by the surface ($\Delta\text{OLR}_{\text{sfc}}(T_i)$, dashed curves in figures 1(b) and (c)) via the term $\bar{\bar{\mathfrak{T}}}\delta B(T_s)$ (figure 1(d)).

In the next section, we investigate the role of the atmospheric contribution on the observed OLR–T_s relationship, based on the regions with T_s above 270 K (89% of the surface area). Over this T_s range, the linear regression slope is 2.11 and 2.24 W m^{-2} K^{-1} for clear- and all-sky conditions respectively. Section 3.1 focuses on the clear-sky OLR and conducts experiments to identify key atmospheric conditions that contribute to the linear regression slope and the curvature as observed in figure 1(b) for clear-sky OLR. Section 3.2 further discusses the cloud effects in amplifying the atmospheric contribution and shaping the all-sky OLR shown in figure 1(a).

3. How atmosphere shapes the OLR–T_s relationship

3.1. Clear-sky

While the surface contribution to clear-sky OLR, which can be directly computed from radiative transfer models, fails to effectively explain the observed OLR–T_s relationship, the atmospheric contribution poses a challenge due to the interplay between transmission, emission, and perturbations to them. Alternatively, we infer the sum of atmospheric contributions from the OLR increase not explained by $\Delta \mathrm{OLR_{sfc}}$ as $\Delta \mathrm{OLR_{atm}}$:

$$\Delta \mathrm{OLR}\,(T_i) = \mathrm{OLR}\,(T_s = T_i) - \mathrm{OLR}\,(T_s = 270)$$
$$\Delta \mathrm{OLR_{atm}}\,(T_i) = \Delta \mathrm{OLR}\,(T_i) - \Delta \mathrm{OLR_{sfc}}\,(T_i). \tag{4}$$

Figure 2 shows the $\Delta \mathrm{OLR_{cs}}$, $\Delta \mathrm{OLR_{cs,sfc}}$, and $\Delta \mathrm{OLR_{cs,atm}}$ based on monthly-mean reanalysis dataset in black curves, with respect to 270 K T_s; similar results but with respect to 220 K are shown in figure B2. In the 270 to 305 K T_s range, the clear-sky OLR–T_s slope is at 2.11 W m^{-2} K^{-1} (figure 2(a)), and 1.27 W m^{-2} K^{-1} of it is explained by the surface term (figure 2(b)). Figure 2(c) reveals that the atmospheric term not only contributes to 0.85 W m^{-2} K^{-1} of the linear slope but also controls the curved OLR–T_s relationship.

Earlier studies [13] have depicted a 'radiator fin' in dry, descending regions and a 'radiator furnace' in moist, ascending regions, which highly aligns with the key feature observed in figure 1. The proposed explanation was that higher OLR occurs in drier regions because the atmosphere is more transparent in the longwave spectrum with less water vapor content, allowing for more efficient heat loss to space [13]. Thus it would appear that the transmittance of the entire atmospheric column ($\bar{\bar{\mathfrak{T}}}$ and $\delta\bar{\bar{\mathfrak{T}}}$) might explain the observed OLR–T_s curve. On the other hand, it is well-known that OLR is quantitatively sensitive to layer-by-layer perturbations in atmospheric humidity [5–7, 9, 11, 12, 17]. However, it is unclear

whether the OLR sensitivities to the humidity perturbations in global-mean or local grid points would lead to a conclusion that differs from the first-order picture in which transmission through the entire atmospheric column shapes the OLR–T_s relationship.

To understand how the complex atmospheric properties shape the observed OLR–T_s relationship, we construct a set of atmospheric columns using the ERA5 reanalysis dataset. At each 1 K T_s bin, we build three cases, as summarized in table 1, that have identical temperature and ozone profiles, well-mixed greenhouse gas contents, stratospheric water vapor, and column-integrated water vapor in the troposphere (CIWV), but distribute CIWV differently in vertical levels.

In case (a), the tropospheric relative humidity (RH) is fixed at 40%, while the bottom layer humidity is adjusted to achieve the prescribed CIWV. Case (b) assumes vertically-uniform tropospheric RH within each T_s bin, with the RH values inferred from the prescribed CIWV. Case (c) utilizes the mean RH profile at each T_s bin derived from ERA5 and should largely reproduce the mean OLR of each bin. Given that the transmittance through the entire atmospheric column ($\bar{\bar{\mathfrak{T}}}$) is primarily controlled by water vapor [23] via CIWV, we expect $\bar{\bar{\mathfrak{T}}}$ and changes in transmittance ($\delta\bar{\bar{\mathfrak{T}}}$) to be similar across these different cases.

Following this idea, we conduct clear-sky radiative transfer calculations for three cases at every T_s bin using MODTRAN 5.2 [24] (see appendix A) to derive the OLR–T_s relationship, $\Delta \mathrm{OLR_{cs}}$ (figure 2(a)), the surface component, $\Delta \mathrm{OLR_{cs,sfc}}$ (figure 2(b)), and the atmospheric component, $\Delta \mathrm{OLR_{cs,atm}}$ (figure 2(c)). As expected, the surface component overlaps among the three cases, primarily owing to the dominant impact of CIWV on the magnitude of $\bar{\bar{\mathfrak{T}}}$, further suggesting the similarity of $\delta\bar{\bar{\mathfrak{T}}}$ across these cases. Consequently, any discrepancies observed in the OLR–T_s relationship among the three cases can be attributed solely to changes in atmospheric emission. These OLR–T_s relationships and their differences are used to elucidate how atmospheric conditions shape the slope and curvature observed in the OLR–T_s relationship.

3.1.1. Atmospheric emission maintains the near-constant $\partial \mathrm{OLR_{cs}}/\partial T_s$

Figure 2(a) shows that the observed OLR–T_s slope is much steeper than the surface component (figure 2(b)) could explain, even in case (a) when a constant tropospheric RH is maintained. This result should not be taken for granted because it breaks 'Simpson's law' suggested by previous studies [18, 25], which states that if the water vapor mass at any given temperature level is constant (i.e. constant RH) regardless of T_s, then thermal emission from water
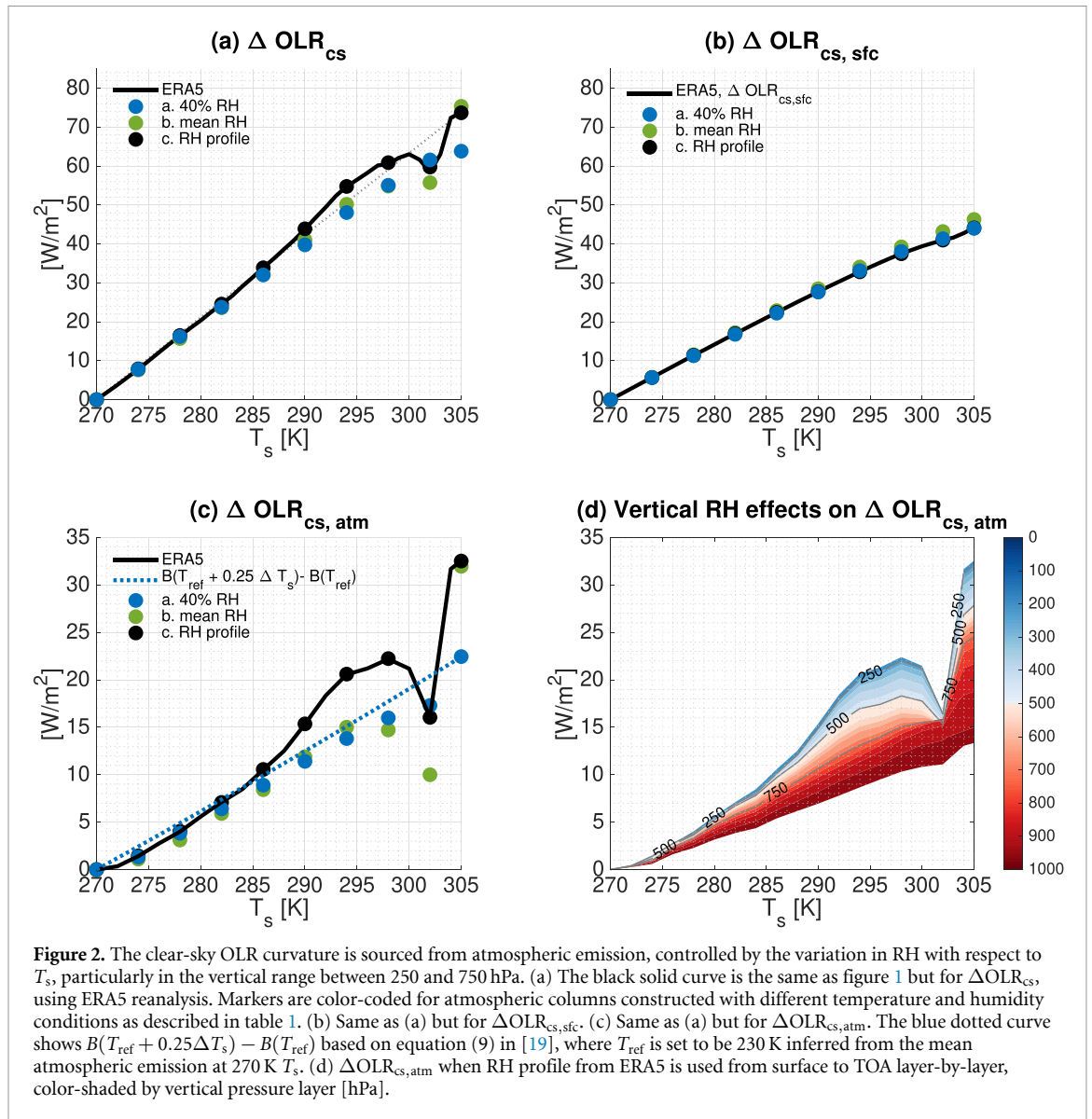
Figure 2. The clear-sky OLR curvature is sourced from atmospheric emission, controlled by the variation in RH with respect to T_s, particularly in the vertical range between 250 and 750 hPa. (a) The black solid curve is the same as figure 1 but for ΔOLR_{cs}, using ERA5 reanalysis. Markers are color-coded for atmospheric columns constructed with different temperature and humidity conditions as described in table 1. (b) Same as (a) but for $\Delta OLR_{cs,sfc}$. (c) Same as (a) but for $\Delta OLR_{cs,atm}$. The blue dotted curve shows $B(T_{ref} + 0.25\Delta T_s) - B(T_{ref})$ based on equation (9) in [19], where T_{ref} is set to be 230 K inferred from the mean atmospheric emission at 270 K T_s. (d) $\Delta OLR_{cs,atm}$ when RH profile from ERA5 is used from surface to TOA layer-by-layer, color-shaded by vertical pressure layer [hPa].

Table 1. A summary of atmospheric columns constructed at every 1 K surface temperature bin with different vertical distribution of tropospheric humidity. Temperature profiles, well-mixed greenhouse gases, O_3, and tropospheric column-integrated water vapor (CIWV), and stratospheric humidity (above 200 hPa) are the same in cases a, b, and c as in ERA5 multi-year-mean. Clear-sky radiative transfer calculations are conducted at every T_s bin using MODTRAN 5.2 [24] at 1 cm^{-1} spectral resolution to obtain ΔOLR_{cs}, $\Delta OLR_{cf,sfc}$, and $\Delta OLR_{cs,atm}$ presented in figure 2. ΔOLR_{sfc}, and $\Delta OLR_{cs,atm}$ are used to derive the linear regression slope ($\partial OLR_{cs,sfc}/\partial T_s$ and $\partial OLR_{cs,atm}/\partial T_s$) and are presented in this table.

| Experiments	Temperature	Humidity	$\partial \mathbf{OLR_{cs,sfc}}/\partial \mathbf{T_s}$	$\partial \mathbf{OLR_{cs,atm}}/\partial \mathbf{T_s}$
Atmospheric columns with different tropospheric humidity				
a. 40% RH	Multi-year-mean within each T_s bin figure B4(b)	Prescribed CIWV 40% tropospheric RH (except for the bottom layer)	1.30 W m^{-2} K^{-1}	0.62 W m^{-2} K^{-1}
b. Mean RH	Figure B4(b)	Prescribed CIWV Vertically-uniform RH in the troposphere Green curve in figure B4(a)	1.34 W m^{-2} K^{-1}	0.70 W m^{-2} K^{-1}
c. RH profile	Figure B4(b)	Vertically-resolved tropospheric RH	1.27 W m^{-2} K^{-1}	0.87 W m^{-2} K^{-1}
ERA5	—	—	1.27 W m^{-2} K^{-1}	0.85 W m^{-2} K^{-1}
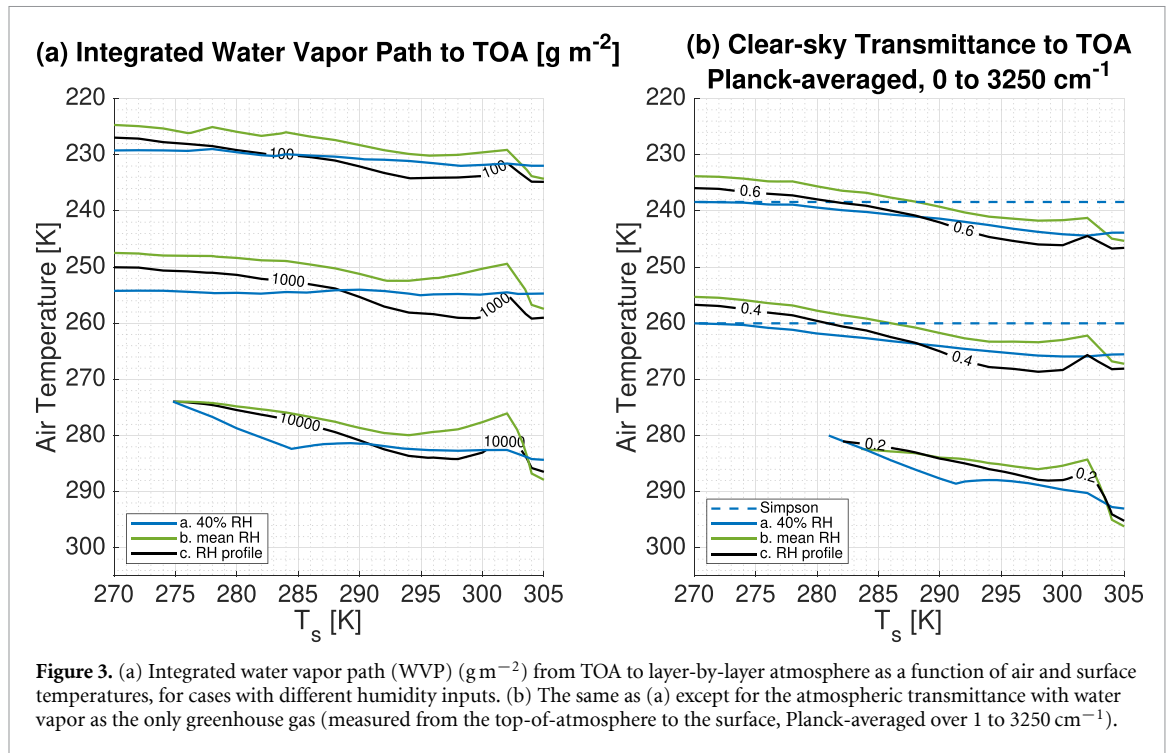
Figure 3. (a) Integrated water vapor path (WVP) $(g\,m^{-2})$ from TOA to layer-by-layer atmosphere as a function of air and surface temperatures, for cases with different humidity inputs. (b) The same as (a) except for the atmospheric transmittance with water vapor as the only greenhouse gas (measured from the top-of-atmosphere to the surface, Planck-averaged over 1 to 3250 cm^{-1}).

vapor should be largely constant even when the surface warms. Figure 3(a) shows that case (a) maintains a near-constant water vapor path (WVP) at temperature levels, but $\Delta OLR_{cs,atm}$ still increases significantly with T_s (figure 2(b)). A similar magnitude in $\Delta OLR_{cs,atm}$ is found even when water vapor is held as the only greenhouse gas in figure B3 for an idealized scenario constructed in table C1.

To understand why $\Delta OLR_{cs,atm}$ increases with T_s, we examine the opacity of water vapor of case (a) in figure 3(b). It shows that with constant RH, $\Delta OLR_{cs,atm}$ increases with T_s because the opacity of water vapor is not constant for the same mass of water vapor. Simpson's law would only hold if specific humidity is invariant with T_s on both temperature (i.e. by holding RH) and pressure coordinates. This necessitates that temperature profiles from various T_s perfectly overlap in a pressure coordinate. As an example, in table C1 and figure B3(c), a hypothetical scenario 'Simpson' is constructed by extending the temperature–pressure profile at 270 K T_s to warmer temperatures and higher pressure levels. This scenario maintains zero $\Delta OLR_{cs,atm}$ (figure B3(a)), but requires an unrealistic increase in surface pressure with respect to T_s. Because the surface air pressure is relatively constant across T_s, as opposed to 'Simpson' (figure B3(c)), a foreign pressure effect on the thermal emission of water vapor is introduced, reducing the extinction efficiency per unit mass at a given air temperature [19, 26, 27]. Consequently, the opacity contour shifts to warmer atmospheric layers

(figure 3(b)), leading to an increase in $\Delta OLR_{cs,atm}$ with T_s. The effective emission temperature of the atmosphere follows this shift and increases by approximately 0.25 K for every 1 K increase in T_s (25% of ΔT_s). This rate of emission temperature shift is determined by the Clausius–Clapeyron equation and the hydrostatic balance [28], as demonstrated in equation (9) of [19]. Therefore, $\Delta OLR_{cs,atm}$ increases with T_s in case (a) due to changes in emission temperature. $\Delta OLR_{cs,atm}$ appeared to be linearly dependent on T_s because the dampened emission temperature shift (25%) cancels out the growth curve in $B(T_s)$, making the observed OLR–T_s relationship much steeper and much more linear than the surface contribution could explain (figures 1(b)–(d)).

3.1.2. Atmospheric emission shapes the clear-sky OLR–T_s relationship via relative humidity distribution

However, case (a) cannot reproduce the curved OLR–T_s relationship even with its total atmospheric transmittance matching the reanalysis. The big discrepancies between case (a) and other cases with the same CIWV but varying humidity profile preclude any major effects from the trapping greenhouse effect of water vapor (via $\bar{\mathfrak{T}}$ and $\delta\bar{\mathfrak{T}}$), suggesting that the atmospheric emission must have played a key role in shaping the observed OLR–T_s curve.

Figure 2 demonstrates that the curved OLR–T_s relationship is better captured in case (b), where RH is uniformly prescribed in every tropospheric layer to yield the mean CIWV at each T_s bin. With

the moister tropospheric-mean RH at 302 K than at 298 K (green curve in figure B4(a)), the transmittance contour is lifted to colder temperature layers from 298 to 302 K (green in figure 3(b)). Therefore, OLR at 302 K is lower than 298 K because atmospheric emission at colder layers contributes to OLR more effectively in moist regions (302 K) than in dry regions (298 K).

Surprisingly, with the vertically uniform tropospheric RH simplification, case (b) cannot fully explain the linear slope in $\Delta OLR_{cs,atm}$ (figure 2(c)). It underestimates the overall ΔOLR_{cs} and fails to account for the maximum $\Delta OLR_{cs,atm}$ occurring at 298 K instead of 294 K, where the mean tropospheric RH is the lowest (figure B4(a)). Case (c) eliminates these discrepancies by using a vertically-resolved RH profile in the troposphere at each T_s bin. Figure 2(d) shows that the WVP with respect to air temperature levels reaches a minimum at 298 K, and the contour curves in the mid-troposphere (around 240 to 270 K air temperature levels or 250 to 750 hPa pressure levels) are much steeper than the average troposphere. It suggests that the mean tropospheric RH in Case (b) inadequately represents the humidity change in the mid-troposphere.

By considering contributions from realistic RH layer-by-layer from the surface to the TOA and conducting radiative transfer calculations, we demonstrate in figure 2(d) that the mid-troposphere (between 250 and 750 hPa) significantly influences both the slope and intensity of the $\Delta OLR_{cs,atm}-T_s$ curve. While previous studies have recognized the importance of mid-tropospheric humidity using radiative partial perturbation methods and kernels [7, 11, 12], the radiative transfer through the constructed columns proves that the mid-tropospheric humidity is important because it determines the atmospheric emission to space. The importance of mid-tropospheric RH shown here also explains why the OLR–T_s relationship appears more linear when grids with conserved mid-tropospheric RH, rather than boundary-layer RH, are chosen [3].

In summary, we find that the surface contribution alone is insufficient to describe the clear-sky OLR–T_s relationship (figure 2(b) versus figure 2(a)). On the one hand, a significant fraction (approximately 40%) of the linear slope in the observed OLR–T_s relationship is attributable to atmospheric thermal emission, primarily from water vapor (figure B3(a)), which is induced by the foreign pressure effect and enhanced by variations in tropospheric RH. On the other hand, the curved shape in the OLR–T_s relationship is predominantly due to atmospheric emission: OLR peaks at 298 K because this 1 K surface temperature bin on average corresponds to the driest mid-troposphere, allowing for more effective emission from warmer atmospheric layers rather than just the surface. These key characteristics of

the clear-sky OLR–T_s relationship cannot be reproduced without considering the vertical distribution of RH.

3.2. All-sky
Based on similar approaches conducted in section 3, figure 4(a) shows that the all-sky OLR–T_s curve (ΔOLR) is quite similar to clear-sky, with comparable magnitudes of linear slope for the 270 to 305 K T_s range, and a similar curved shape that deviates from the linear slope among CMIP6 models and the reanalysis. The ΔOLR_{sfc} of ERA5 is computed using the all-sky total atmospheric transmittance and shown in figure 4(b) based on GRTCODE.

With cloud masking effects, ΔOLR_{sfc} can only explain 27% of the slope in the OLR–T_s relationship (the solid curve with markers in figure 4(b)). The OLR–T_s slope stays comparable to that in the clear-sky because ΔOLR_{atm} is greatly enhanced by clouds and compensates for the masked surface contribution (the solid curve in figure 4(b)).
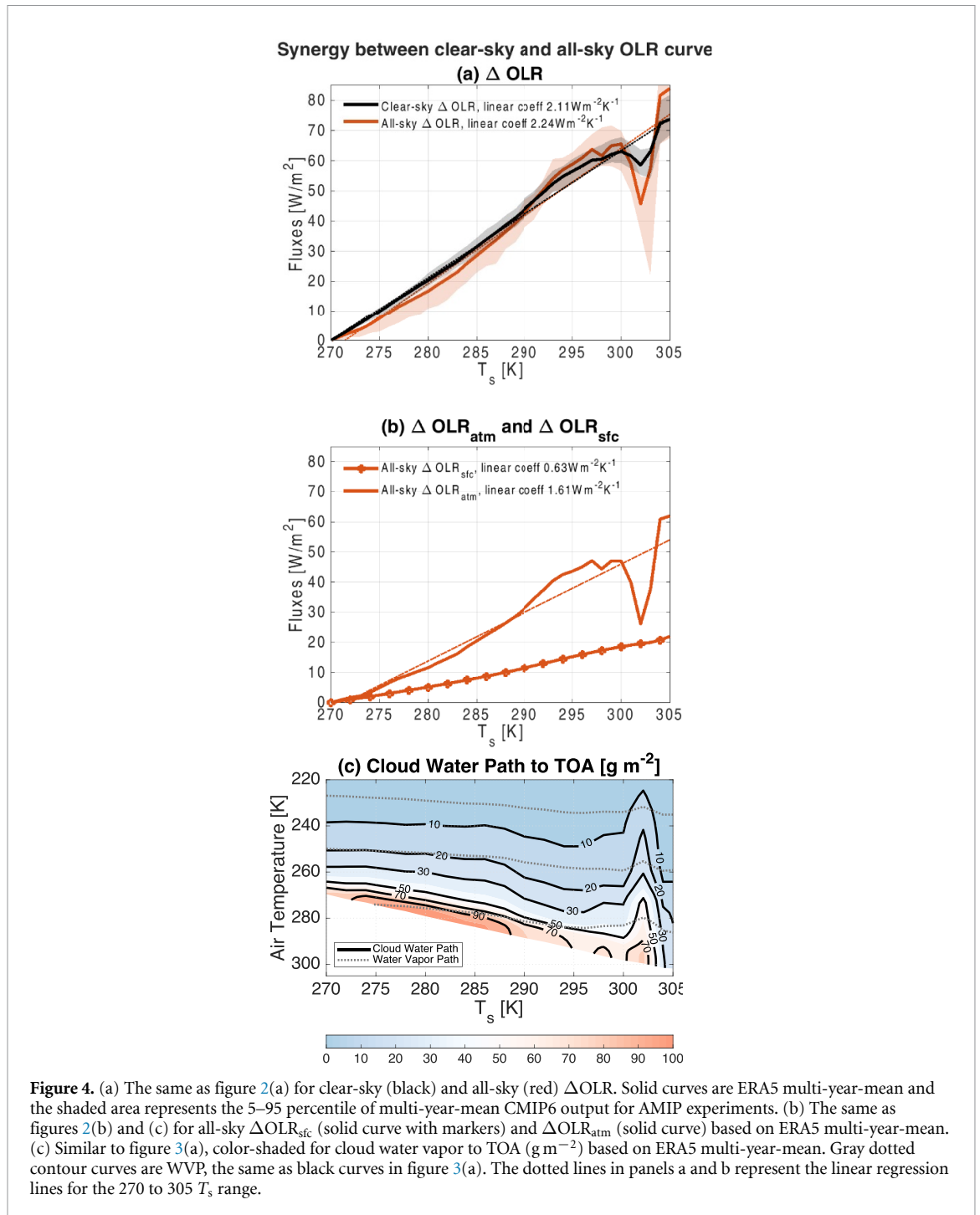
Furthermore, we show that clouds are in synergy with water vapor when contributing to the atmospheric emission. With decreasing RH with T_s from 270 K T_s to the subtropical region (as evidenced by the green curve in figure B4(a) and the dotted curves in figure 4(c)), a simultaneous reduction in cloud water path is observed (solid curves in figure 4(c)). This reduction in the cloud water path contributes to the enhancement of the OLR curve within the 270 to 298 K T_s range. Meanwhile, the cloud water path reaches a maximum at 302 K, amplifying the OLR dip (the red curve in figure 4(a) and the solid curve in panel (b)) in this moist, convective region.

In conclusion, the atmospheric contribution to the OLR–T_s relationship is more dominant in all-sky conditions and is largely explained by the co-variation of clouds and humidity with T_s.

4. The cause of inter-model spread in the clear-sky OLR curve

Figure 5(a) shows the mean clear-sky OLR at each T_s bin from the AMIP simulation of 24 CMIP6 models (see appendix A). For every model, deviations from multi-model-mean clear-sky OLR at every given 1 K T_s bin are shown in the y-axis of figure 5(e). These deviations are used to quantify the inter-model spread found in figure 5(a) and are up to $\pm10\,\mathrm{W\,m^{-2}}$, which is surprisingly large with the prescribed sea surface temperature in the AMIP experiment. In this section, the cause of inter-model spread in clear-sky OLR at given T_s is examined.

In particular, it is intriguing to decompose whether the spread is caused by differences in radiative transfer schemes used by these models or by differences in atmospheric states. Therefore, we perform global clear-sky radiative transfer calculations for 24 CMIP6 models using RTE-RRTMGP [29], as

Figure 4. (a) The same as figure 2(a) for clear-sky (black) and all-sky (red) ΔOLR. Solid curves are ERA5 multi-year-mean and the shaded area represents the 5–95 percentile of multi-year-mean CMIP6 output for AMIP experiments. (b) The same as figures 2(b) and (c) for all-sky ΔOLR$_{sfc}$ (solid curve with markers) and ΔOLR$_{atm}$ (solid curve) based on ERA5 multi-year-mean. (c) Similar to figure 3(a), color-shaded for cloud water vapor to TOA (g m^{-2}) based on ERA5 multi-year-mean. Gray dotted contour curves are WVP, the same as black curves in figure 3(a). The dotted lines in panels a and b represent the linear regression lines for the 270 to 305 T_s range.

described in appendix A. The multi-year-mean OLR and transmittance at every model grid point are computed from monthly-mean results. This set of calculations excludes any discrepancies induced by the treatment of greenhouse gases and biases in radiative transfer schemes. The spread in clear-sky OLR at each 1 K T_s bin computed from RRTMGP remains comparable to the standard output from CMIP6 (i.e. *y*-axis of figure B5(c) compared to figure 5(e)), suggesting a large fraction of the inter-model spread is caused by discrepancies in atmospheric states.

Overall, these models exhibit curved shapes in OLR that are highly consistent with ERA5, reaching a maximum around 298 K and a dip around 302 K. However, the strength of this OLR curvature, evaluated as the OLR contrast between the two T_s bins, is quite different across models, as shown in the y axes of figures 5(b)–(d), ranging from −0.3 to 4 W m^{-2}. The region between 298 and 302 K spans over the majority of the subtropical and tropical ocean (figure B1), and is representative of the most dramatic changes in humidity conditions with T_s over the present-day Earth. The magnitude of OLR contrast between the
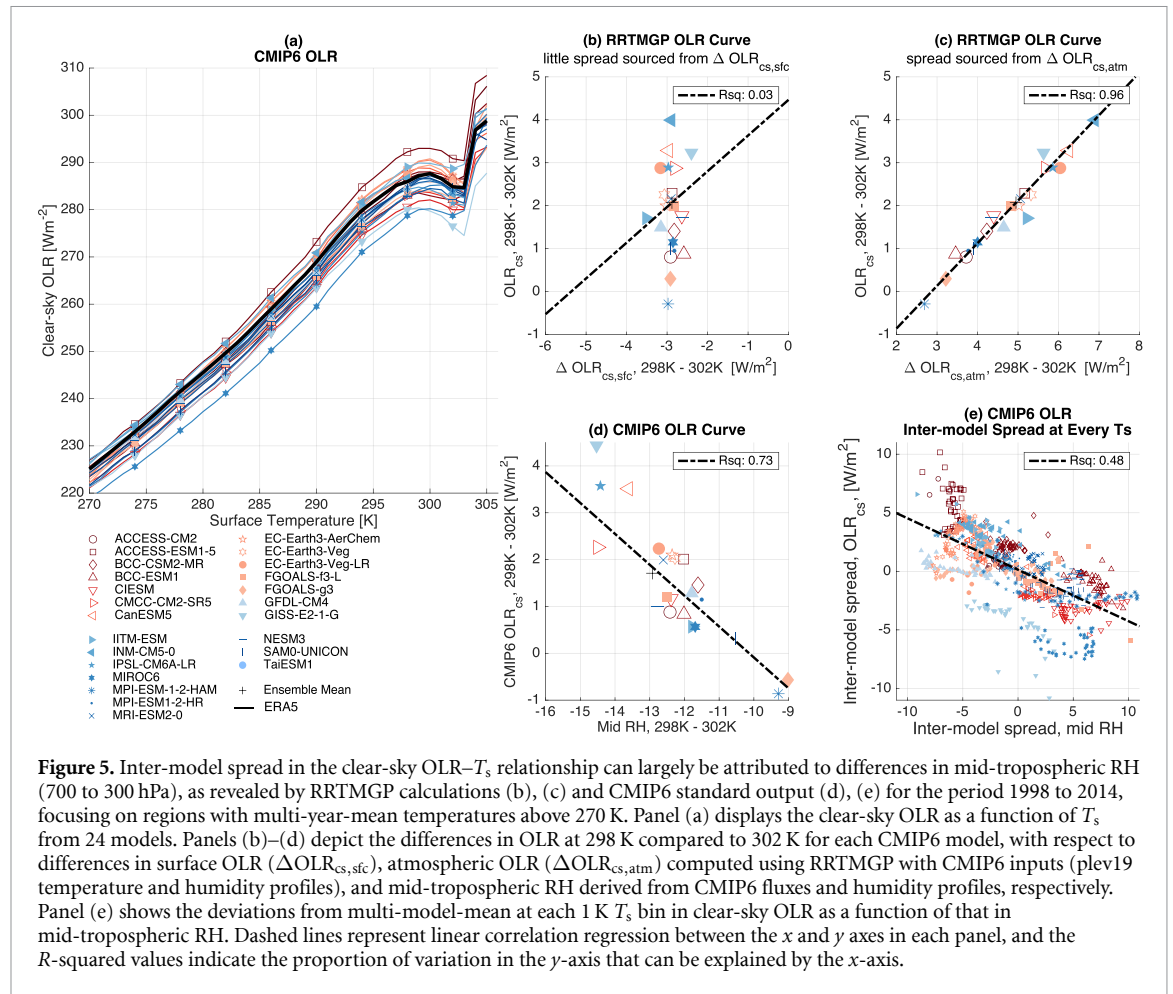
Figure 5. Inter-model spread in the clear-sky OLR–T_s relationship can largely be attributed to differences in mid-tropospheric RH (700 to 300 hPa), as revealed by RRTMGP calculations (b), (c) and CMIP6 standard output (d), (e) for the period 1998 to 2014, focusing on regions with multi-year-mean temperatures above 270 K. Panel (a) displays the clear-sky OLR as a function of T_s from 24 models. Panels (b)–(d) depict the differences in OLR at 298 K compared to 302 K for each CMIP6 model, with respect to differences in surface OLR ($\Delta OLR_{cs,sfc}$), atmospheric OLR ($\Delta OLR_{cs,atm}$) computed using RRTMGP with CMIP6 inputs (plev19 temperature and humidity profiles), and mid-tropospheric RH derived from CMIP6 fluxes and humidity profiles, respectively. Panel (e) shows the deviations from multi-model-mean at each 1 K T_s bin in clear-sky OLR as a function of that in mid-tropospheric RH. Dashed lines represent linear correlation regression between the x and y axes in each panel, and the R-squared values indicate the proportion of variation in the y-axis that can be explained by the x-axis.

two bins indicates how each model represents the tropical circulation that transports heat and moisture between the moist, ascending 'radiator furnace' and the dry, descending 'radiator fin' on Earth [13].

Based on RRTMGP calculations and following section 3, we break down the contribution to the OLR contrast between 298 and 302 K region into the surface ($\Delta OLR_{cs,sfc}$) and atmospheric contributions ($\Delta OLR_{cs,atm}$), as shown in figures 5(b) and (c). While the consistency in $\Delta OLR_{cs,sfc}$ across models suggests an overall good agreement in the CIWV, the changes in atmospheric emission do not align well among the CMIP6 models when using the same radiative transfer codes. Combing figures 5(b) and (c), our results suggest that the inter-model spread in the strength of OLR curvature is primarily sourced from atmospheric emission, potentially due to the mid-tropospheric RH as alluded to in section 3.1.2.

Next, we examine whether the inter-model spread in clear-sky OLR can be explained by the mid-tropospheric RH. Figure 5(d) shows that 73% of the inter-model spread in the clear-sky OLR difference between the 298 K and 302 K regions can be attributed to the inter-model spread in mid-tropospheric RH. If the contrast in the mid-tropospheric RH is too low in one model, the model tends to

produce a relatively low or even negative OLR contrast between the subtropical ocean at 298 K and the tropical warm pool at 302 K, due to compensation from the $\Delta OLR_{cs,sfc}$ term at $-3\,W\,m^{-2}$. Meanwhile, models with excessively high RH contrast overestimate the OLR contrast between the two regions.

Furthermore, for every 1 K T_s bin, the departure from multi-model-mean in mid-tropospheric RH (x-axis of figure 5(e)) explains 48% of the inter-model spread in clear-sky OLR (as seen in figure 5(a) and evaluated in the y-axis of figure 5(e)). It suggests that lower clear-sky OLR at a given surface temperature in one model is most likely due to a moister mid-troposphere RH in this model; this finding is consistent with recent studies on the cause of spread in global-mean OLR [30].

5. Discussion

This study reveals a robust and curved relationship between OLR and surface temperature (T_s) in CMIP6 models and ERA5 reanalysis datasets. While the OLR–T_s relationship appears linear within a wide T_s range (220 K to 305 K), this masks the uneven distribution of T_s across the globe and the deviation of OLR from

a simple linear relationship in the warmer regions of Earth's surface under both clear- and all-sky conditions. By constructing atmospheric columns based on ERA5 multi-year-mean data, our results explain the key feature in the observed clear-sky OLR–T_s relationship.

First, the overall linearity observed in the clear-sky OLR–T_s relationship is regulated by both the surface and the atmosphere. On the one hand, the infrared opacity of water vapor throughout the atmospheric column, as noted in [2], controls the rate at which surface thermal emission escapes to space (black curve between 220 and 280 K T_s in figure 1(d); the term $\overline{\mathfrak{T}}\delta B(T_s)$ in equation (2)). On the other hand, the emission temperature from water vapor itself tends to increase by 0.25 K per 1 K of increase of T_s (under fixed RH, blue solid and dotted lines in figure 2(c); the second term on the right-hand side of equation (2)), a rate jointly determined by the Clausius–Clapeyron relation on water vapor mass and a foreign pressure effect on water vapor extinction efficiency, as explained in [19]. Because water vapor mass increases exponentially with temperature and effectively offsets the quadratic growth curve in blackbody thermal emission, both the surface and the atmosphere can contribute to the linear OLR slope, with their magnitudes compensating for each other depending on atmospheric opacity. In colder and drier regions, the surface contribution is dominant, while in warmer and moister regions, the atmospheric contribution becomes more significant. This finding aligns with previous studies by [19, 31]. On the present-day Earth, the surface contribution accounts for 60% and the atmospheric emission via foreign pressure effect accounts for 30% of the linear slope in the observed clear-sky OLR–T_s relationship.

Second, the variability in tropospheric RH in the mid-troposphere (250–750 hPa vertical range) has a substantial impact on atmospheric thermal emission and contributes to an additional 10% increase in OLR with T_s. Moreover, the spatial variations in mid-tropospheric humidity play a crucial role in the observed non-linearity of the OLR–T_s relationship over the subtropical and tropical oceans, as illustrated in figures 2(c) and (d), resulting from the large-scale tropical circulation [13]. We find that OLR over the dry subtropical ocean (around 298 K T_s) is higher than over the moist tropical ocean (around 302 K T_s) because the drier mid-troposphere shifts atmospheric emission to warmer layers (figure 3(b)), rather than reducing the trapping of surface thermal emission.

Furthermore, our results reveal that CMIP6 models have a remarkable wide spread (up to 10 W m^{-1}) in climatological clear-sky OLR at given sea surface temperatures in AMIP simulations (figures 5(a) and (e)). The main cause of the spread (for regions warmer than 270 K) is found to be model biases in mid-tropospheric RH (figures 5(c) and (d)), which can be affected by discrepancies in land surface temperature, microphysics and convective parameterization across models. In addition, we find that a few CMIP6 models may be biased in radiation parameterization, as it clearly diverges from other CMIP6 models (figure 5(e)) and RRTMGP-computed fluxes (figure B5(c)). These biases should be carefully examined in the future.

Finally, we find that the all-sky OLR–T_s relationship exhibits a comparable linear slope but much stronger deviations from the linearity (figure 4(a)). While clouds act to mask over the surface contribution to OLR–T_s slope (0.63 W m^{-2} K^{-1}, figure 4(b)), it significantly amplifies the OLR sensitivity to atmospheric thermal emission. In all-sky conditions, the atmospheric contribution to OLR–T_s slope is enhanced to 1.61 W m^{-2} K^{-1}, compensates for the masked surface contribution, maintaining comparable linear slope to the clear-sky conditions. Because clouds and water vapor are strongly correlated (figure 4(c)), variation of clouds with T_s induces similar but stronger deviations from the linear relationship. The synergy between clear- and all-sky OLR–T_s relationships indicates that the general circulation from the tropics to poles and across the tropical ocean is important for redistributing the atmospheric energy and moisture to maintaining the observed OLR–T_s relationship in Earth's climate [13, 32, 33].

Data availability statement

Acknowledgments

Appendix A. Data and method

This study uses ERA5 reanalysis [22] and CMIP6 model AMIP simulations [34] to examine what shapes the overall OLR–T_s relationship over the present-day Earth, based on the period from 1998 to 2014. The AMIP simulation is an atmosphere-only climate simulation using prescribed sea surface temperature and sea ice concentrations, and historical well-mixed greenhouse gas concentrations.

While OLR fluxes from reanalysis and model outputs are used, we also conduct radiative transfer calculations to explicitly calculate atmospheric transmission of surface emission and atmospheric emission. Three sets of radiative transfer models are used to balance the need for accuracy and efficiency. Monthly-mean ozone profiles and well-mixed greenhouse gas concentrations are used in these models if not otherwise specified. Temperature and humidity profiles from ERA5 and CMIP6 models at every grid point are used to drive the radiative transfer calculations. They consist of 37 model levels for ERA5 and 19 pressure levels for CMIP6 models.
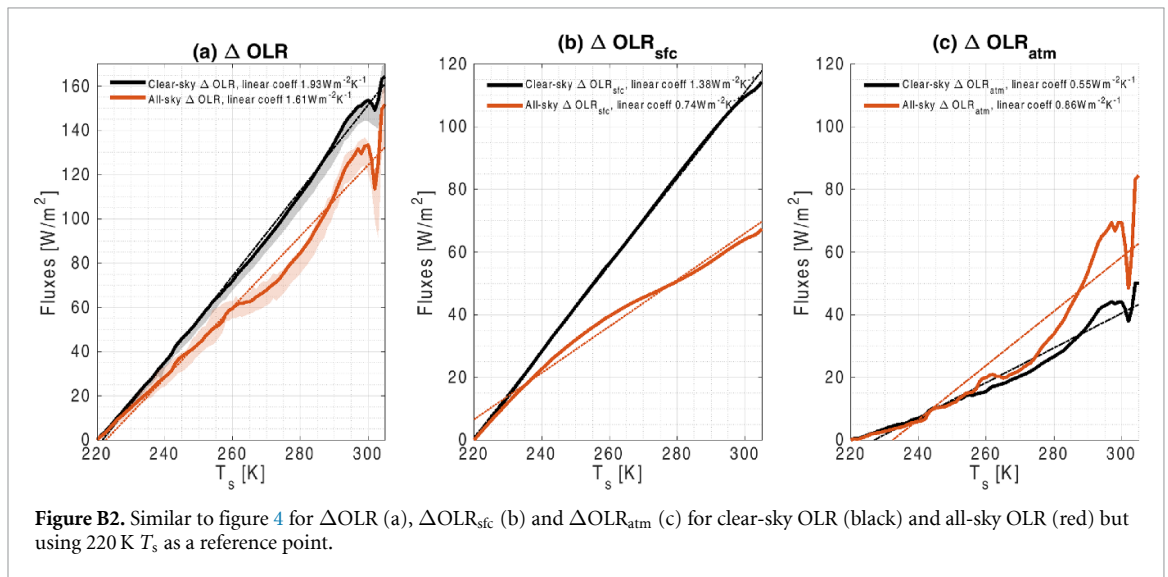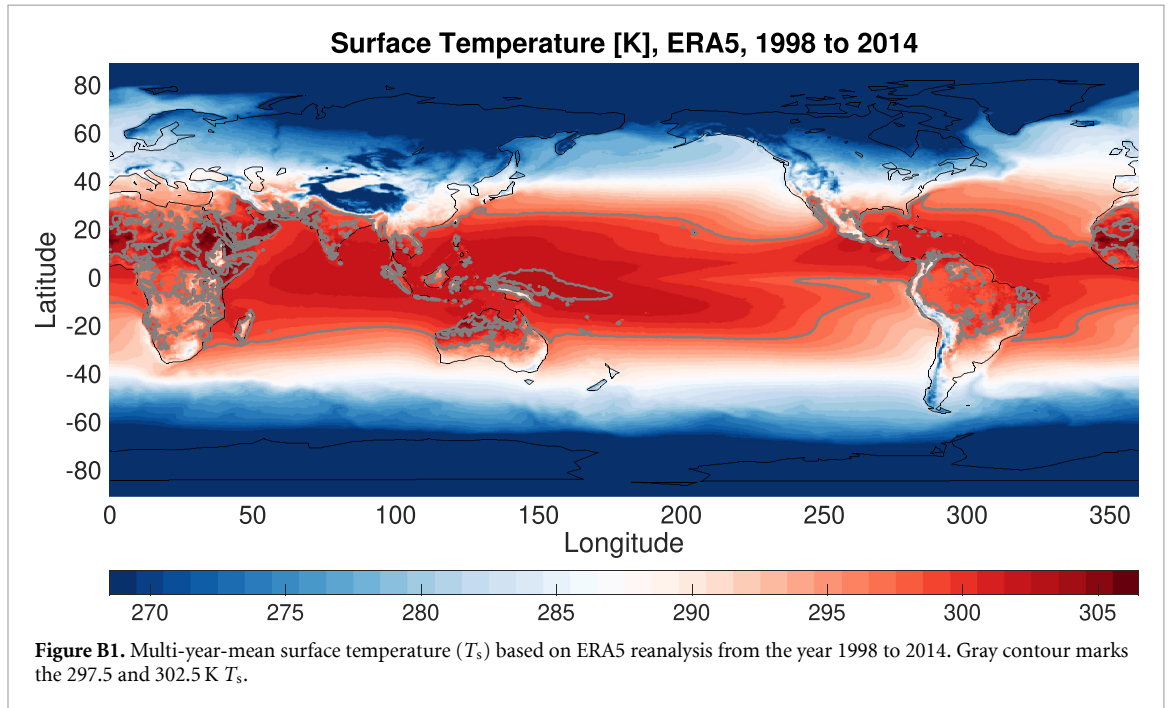
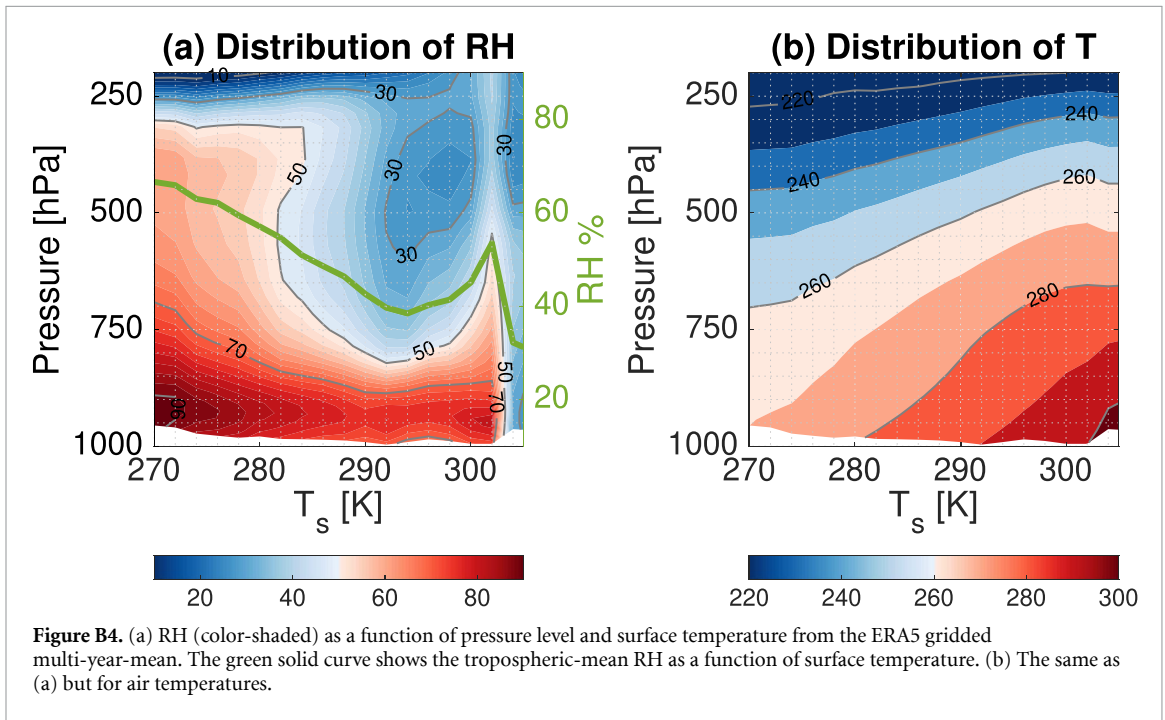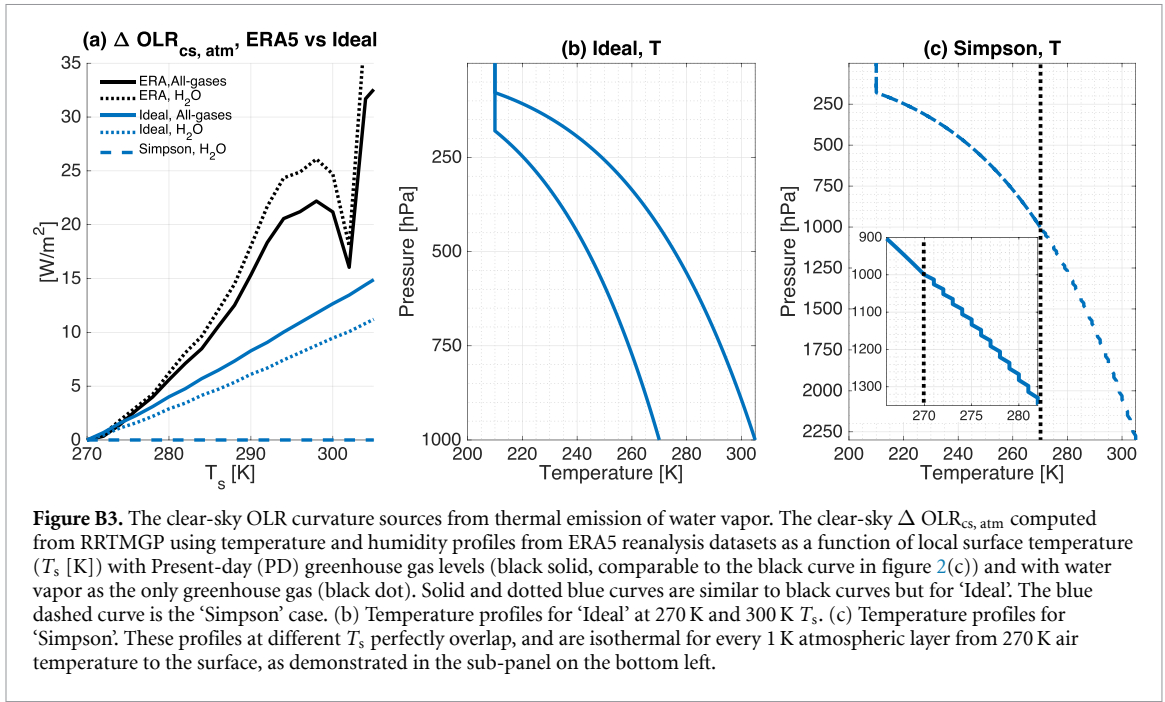Geophysical Fluid Dynamics Laboratory's GPU-able Radiative Transfer code (GRTCODE) is a well-benchmarked [35] line-by-line code. It is used to set up a benchmark value for atmospheric transmittance over the present-day Earth. Clear-sky fluxes are computed at every grid point from the year 1998 to 2014 with monthly-mean temperature and humidity profiles from the reanalysis. Ten sub-columns per grid box are stochastically generated from cloud inputs [36, 37]. Fluxes of each sub-column at each wavenumber are computed, and the all-sky fluxes are computed as the average of the sub-columns.

MODTRAN 5.2 [24] is a fast yet accurate band model that has been widely used in atmospheric radiation studies. It is used to compute atmospheric transmittance at every $1\,\mathrm{cm}^{-1}$ through constructed temperature and humidity profiles at each T_s bin. With identical atmospheric inputs, the difference in atmospheric transmittance between MODTRAN 5.2 and GRTCODE is within 1%.

RTE-RRTMGP [29] is a radiative transfer code designed for fast global-scale radiative transfer calculations. It is used to compute broadband fluxes and transmittance at every grid point with multi-year monthly-mean temperature and humidity profiles from AMIP simulations of 24 CMIP6 models and to analyze the cause of intermodel spread in OLR.

Appendix B. Supplementary figures

Figure B1. Multi-year-mean surface temperature (T_s) based on ERA5 reanalysis from the year 1998 to 2014. Gray contour marks the 297.5 and 302.5 K T_s.

Figure B2. Similar to figure 4 for ΔOLR (a), ΔOLR$_{sfc}$ (b) and ΔOLR$_{atm}$ (c) for clear-sky OLR (black) and all-sky OLR (red) but using 220 K T_s as a reference point.

Figure B3. The clear-sky OLR curvature sources from thermal emission of water vapor. The clear-sky $\Delta OLR_{cs, atm}$ computed from RRTMGP using temperature and humidity profiles from ERA5 reanalysis datasets as a function of local surface temperature (T_s [K]) with Present-day (PD) greenhouse gas levels (black solid, comparable to the black curve in figure 2(c)) and with water vapor as the only greenhouse gas (black dot). Solid and dotted blue curves are similar to black curves but for 'Ideal'. The blue dashed curve is the 'Simpson' case. (b) Temperature profiles for 'Ideal' at 270 K and 300 K T_s. (c) Temperature profiles for 'Simpson'. These profiles at different T_s perfectly overlap, and are isothermal for every 1 K atmospheric layer from 270 K air temperature to the surface, as demonstrated in the sub-panel on the bottom left.

Figure B4. (a) RH (color-shaded) as a function of pressure level and surface temperature from the ERA5 gridded multi-year-mean. The green solid curve shows the tropospheric-mean RH as a function of surface temperature. (b) The same as (a) but for air temperatures.

Figure B5. Same as figures 5(a), (d) and (e) except that OLR fluxes computed from RRTMGP are used.

Appendix C. Supplementary table

Table C1. Similar to table 1 but for idealized atmospheric columns with vertically uniform RH and lapse rate in the troposphere.

Experiments	Temperature	Humidity	$\partial OLR_{cs}, sfc/\partial T_s$	$\partial OLR_{cs}, atm/\partial T_s$
Ideal	Uniform tropospheric lapse rate Surface pressure at 1000 hPa figure B3(b)	40% tropospheric RH	$1.40\,\mathrm{W\,m^{-2}\,K^{-1}}$	$0.43\,\mathrm{W\,m^{-2}\,K^{-1}}$
Simpson	Same as ideal, except that the 270 K air is at 1000 hPa, regardless of the actual T_s figure B3(c)	Same as ideal	$1.25\,\mathrm{W\,m^{-2}\,K^{-1}}$	$0\,\mathrm{W\,m^{-2}\,K^{-1}}$

ORCID iDs

Jing Feng ⬤ https://orcid.org/0000-0003-1144-622X
Chenggong Wang ⬤ https://orcid.org/0000-0003-4147-4686
Raymond Menzel ⬤ https://orcid.org/0000-0002-2459-0119

References

[1] Budyko M I, Yefimova N A, Aubenok L I and Strokina L A 1962 The heat balance of the surface of the earth *Sov. Geogr.* **3** 3–16

[2] Koll D D B and Cronin T W 2018 Earth's outgoing longwave radiation linear due to h2o greenhouse effect *Proc. Natl Acad. Sci.* **115** 10293–8

[3] Zhang Y, Jeevanjee N and Fueglistaler S 2020 Linearity of outgoing longwave radiation: from an atmospheric column to global climate models *Geophys. Res. Lett.* **47** e2020GL089235

[4] Wetherald R T and Manabe S 1988 Cloud feedback processes in a general circulation model *J. Atmos. Sci.* **45** 1397–416

[5] Allan R P, Shine K P, Slingo A and Pamment J A 1999 The dependence of clear-sky outgoing long-wave radiation on surface temperature and relative humidity *Q. J. R. Meteorol. Soc.* **125** 2103–26

[6] Bühler S, Von Engeln A, Brocard E, John V, Kuhn T and Erikson P 2004 The impact of humidity and temperature variations on clear–sky outgoing longwave radiation *J. Geophys. Res.* submitted

[7] Huang Y, Ramaswamy V and Soden B 2007 An investigation of the sensitivity of the clear-sky outgoing longwave radiation to atmospheric temperature and water vapor *J. Geophys. Res.* **112** D05104

[8] Huang Y and Ramaswamy V 2008 Observed and simulated seasonal co-variations of outgoing longwave radiation spectrum and surface temperature *Geophys. Res. Lett.* **35** L17803

[9] Dessler A E, Yang P, Lee J, Solbrig J, Zhang Z and Minschwaner K 2008 An analysis of the dependence of clear-sky top-of-atmosphere outgoing longwave radiation on atmospheric temperature and water vapor *J. Geophys. Res.* **113** D17102

[10] Soden B J, Held I M, Colman R, Shell K M, Kiehl J T and Shields C A 2008 Quantifying climate feedbacks using radiative kernels *J. Clim.* **21** 3504–20

[11] Priyam Raghuraman S, Paynter D and Ramaswamy V 2019 Quantifying the drivers of the clear sky greenhouse effect, 2000–2016 *J. Geophys. Res.* **124** 11354–71

[12] Lang T, Kristin Naumann A, Stevens B and Buehler S A 2021 Tropical free-tropospheric humidity differences and their effect on the clear-sky radiation budget in global storm-resolving models *J. Adv. Model. Earth Syst.* **13** e2021MS002514

[13] Pierrehumbert R T 1995 Thermostats, radiator fins and the local runaway greenhouse *J. Atmos. Sci.* **52** 1784–806

[14] Richards B D G, Koll D D B and Cronin T W 2021 Seasonal loops between local outgoing longwave radiation and surface temperature *Geophys. Res. Lett.* **48** e2021GL092978

[15] Dessler A E, Mauritsen T and Stevens B 2018 The influence of internal variability on earth's energy balance framework and implications for estimating climate sensitivity *Atmos. Chem. Phys.* **18** 5147–55

[16] Bloch-Johnson J, Rugenstein M, Stolpe M B, Rohrschneider T, Zheng Y and Gregory J M 2021 Climate sensitivity increases under higher CO_2 levels due to feedback temperature dependence *Geophys. Res. Lett.* **48** e2020GL089074

[17] Bourdin S, Kluft L and Stevens B 2021 Dependence of climate sensitivity on the given distribution of relative humidity *Geophys. Res. Lett.* **48** e2021GL092462

[18] Jeevanjee N, Koll D D B and Lutsko N 2021 'simpson's law' and the spectral cancellation of climate feedbacks *Geophys. Res. Lett.* **48** e2021GL093699

[19] Feng J, Paynter D and Menzel R 2023 How a stable greenhouse effect on earth is maintained under global warming *J. Geophys. Res.* **128** e2022JD038124

[20] Huang Y, Xia Y and Tan X 2017 On the pattern of CO_2 radiative forcing and poleward energy transport *J. Geophys. Res.* **122** 10 578

[21] Kramer R J, Matus A V, Soden B J and L'Ecuyer T S 2019 Observation-based radiative kernels from CloudSat/CALIPSO *J. Geophys. Res.* **124** 5431–44

[22] Hersbach H *et al* 2020 The ERA5 global reanalysis *Q. J. R. Meteorol. Soc.* **146** 1999–2049

[23] Held I M and Soden B J 2000 Water vapor feedback and global warming *Annu. Rev. Energy Environ.* **25** 441–75

[24] Berk A *et al* 2005 Modtran 5: a reformulated atmospheric band model with auxiliary species and practical multiple scattering options: update *Algorithms and Technologies for Multispectral, Hyperspectral and Ultraspectral Imagery XI* vol 5806 (SPIE) pp 662–7

[25] Simpson S G C 1928 Some studies in terrestrial radiation *Mem. R. Meteorol. Soc.* **11** 69–95

[26] Goody R M and Yung Y L 1989 *Atmospheric Radiation* (Oxford University Press) p 519

[27] Paynter D J and Ramaswamy V 2011 An assessment of recent water vapor continuum measurements upon longwave and shortwave radiative transfer *J. Geophys. Res.* **116** D20302

[28] Wallace J M and Hobbs P V 2006 *Atmospheric Science: An Introductory Survey* vol 92 (Elsevier)

[29] Pincus R, Mlawer E J and Delamere J S 2019 Balancing accuracy, efficiency and flexibility in radiation calculations for dynamical models *J. Adv. Model. Earth Syst.* **11** 3074–89

[30] Huang H and Huang Y 2023 Diagnosing the radiation biases in global climate models using radiative kernels *Authorea Preprints* **50** e2023GL103723

[31] Koll D D B, Jeevanjee N and Lutsko N J 2023 An analytic model for the clear-sky longwave feedback *J. Atmos. Sci.* **80** 1923–51

[32] Hwang Y-T and Frierson D M W 2010 Increasing atmospheric poleward energy transport with global warming *Geophys. Res. Lett.* **37** L24807

[33] Cai M, Sun J, Ding F, Kang W and Hu X 2023 The quasi-linear relation between planetary outgoing longwave radiation and surface temperature: a climate footprint of radiative and non-radiative processes *J. Atmos. Sci.* **80** 2131–46

[34] Eyring V, Bony S, Meehl G A, Senior C A, Stevens B, Stouffer R J and Taylor K E 2016 Overview of the coupled model intercomparison project phase 6 (CMIP6) experimental design and organization *Geosci. Model Dev.* **9** 1937–58

[35] Pincus R *et al* 2020 Benchmark calculations of radiative forcing by greenhouse gases *J. Geophys. Res.* **125** e2020JD033483

[36] Tompkins A M 2002 A prognostic parameterization for the subgrid-scale variability of water vapor and clouds in large-scale models and its use to diagnose cloud cover *J. Atmos. Sci.* **59** 1917–42

[37] Pincus R, Hemler R and Klein S A 2006 Using stochastically generated subcolumns to represent cloud structure in a large-scale model *Mon. Weather Rev.* **134** 3644–56